Spin-Reorientation-Driven Linear Magnetoelectric Effect in Topological Antiferromagnet Cu3TeO6

Virna Kisiček, Damir Dominko, Matija Čulo, Zeljko Rapljenovic, Marko Kuveždić, Martina Dragicevic, Helmuth Berger, Xavier Rocquefelte, Mirta Herak, Tomislav Ivek

Spin-Reorientation-Driven Linear Magnetoelectric Effect in Topological Antiferromagnet Cu_3TeO_6

Virna Kisiček,[1,2,*] Damir Dominko,[1] Matija Čulo,[1] Željko Rapljenović,[1] Marko Kuveždić,[3] Martina Dragičević,[1] Helmuth Berger,[4] Xavier Rocquefelte,[5] Mirta Herak,[1,†] and Tomislav Ivek[1]

[1] *Institute of Physics, Bijenička cesta 46, 10 000 Zagreb, Croatia*
[2] *Faculty of Physics, University of Rijeka, Radmile Matejčić 2, 51 000 Rijeka, Croatia*
[3] *Department of Physics, Faculty of Science, University of Zagreb, Bijenička cesta 32, 10 000 Zagreb, Croatia*
[4] *Institute of Physics, Ecole Polytechnique Fédérale de Lausanne (EPFL), CH-1015 Lausanne, Switzerland*
[5] *Univ Rennes, CNRS, ISCR (Institut des Sciences Chimiques de Rennes) UMR 6226, F-35000 Rennes, France*

(Dated: February 29, 2024)

The search for new materials for energy-efficient electronic devices has gained unprecedented importance. Among the various classes of magnetic materials driving this search are antiferromagnets, magnetoelectrics, and systems with topological spin excitations. Cu_3TeO_6 is a material that belongs to all three of these classes. Combining static electric polarization and magnetic torque measurements with phenomenological simulations we demonstrate that magnetic-field-induced spin reorientation needs to be taken into account to understand the linear magnetoelectric (ME) effect in Cu_3TeO_6. Our calculations reveal that the magnetic field pushes the system from the nonpolar ground state to the polar magnetic structures. However, nonpolar structures only weakly differing from the obtained polar ones exist due to the weak effect that the field-induced breaking of some symmetries has on the calculated structures. Among those symmetries is the PT ($\bar{1}'$) symmetry, preserved for Dirac points found in Cu_3TeO_6. Our findings establish Cu_3TeO_6 as a promising playground to study the interplay of spintronics-related phenomena.

Keywords: Magnetoelectrics, cuprates, antiferromagnets with domains, topological antiferromagnets

Antiferromagnetic (AFM) materials are currently a focus of materials research thanks to the fields of spintronics [1] and magnonics [2]. Large exchange interactions between spins in AFM materials yield spin dynamics at terahertz frequencies and no stray fields make them a natural choice for potential applications in ultrafast spintronic devices [3, 4]. The emerging field of topological magnets has a promising potential in information technology. Owing to the robustness against many perturbations these materials offer a route to the more energy-efficient memory devices, while magnetic excitations (e.g. magnons) could be used to transform and process the information [5]. Topological AFM materials within spintronics, promise new applications in the future technologies [6].

Recent interest in cuprates has shown this family offers a vast playground of exotic ground states and phenomena, such as high-temperature superconductivity, magnetic insulating state, layered crystal structure and strong coupling between spins, charge and orbital degrees of freedom [7–11]. Such couplings can lead to ME effect, i.e. appearance of polarization $\mathbf{P}_i = \alpha_{ij}\mathbf{H}_j$ or magnetization $\mu_0\mathbf{M}_j = \alpha_{ji}\mathbf{E}_i$ in a magnetic or electric field, respectively, as defined by ME tensor α_{ij} [12–16]. Magnetoelectrics open a way to possible applications in data processing and data storage [13, 17, 18], but also in the fundamental understanding concerning the opposite requirements for the d-orbital occupancy for the cross-coupling to emerge [11, 18, 19].

In terms of symmetry analysis, the ME effect vanishes in systems with one of the space inversion P ($\bar{1}$) or time reversal T (1') symmetries, while it is permitted in systems with PT symmetry ($\bar{1}'$). Linear ME coupling in these systems may be generated from the well-known spin-driven ferroelectricity mechanisms (exchange striction mechanism, inverse Dzyaloshinskii-Moriya interaction and spin-dependent p-d hybridization) [20–22], unconventional magnetic ordering [23] as well as a few symmetrically distinct multipole moments [16, 22].

Cu_3TeO_6 is a tellurium-based cuprate [8] which crystallizes in a cubic $Ia\bar{3}$ space group [24]. The Cu^{2+} ions carry spin $S = 1/2$ and lead to an AFM ordered ground state (GS) below the Néel temperature $T_N \approx 62\,\mathrm{K}$, described by trigonal magnetic space group $R\bar{3}'$ [25]. The first-nearest-neighbor (NN) interaction between the spins defines a 3D network of corner-sharing hexagons (inset of Fig. 1a). The spins in the AFM state are almost collinear and aligned along one of the ⟨111⟩ directions of the cubic unit cell [25–27] resulting in the presence of multiple AFM domains [28]. Optical measurements have revealed the magnetoelastic effect deep in the AFM state induced by the spin-phonon coupling [29, 30]. Inelastic neutron scattering (INS) [31, 32] confirmed Heisenberg spin model predictions [27] of topological Dirac and nodal line magnons with PT symmetry preserved. The same technique, in combination with thermodynamic studies, revealed magnon-polaron mode representing the collective excitations resulting from the magnon-phonon coupling [33, 34]. Moreover, a unique magnetic lattice of Cu_3TeO_6 was proposed to be at the origin of the spin gap observed in the nuclear magnetic resonance measurements [35].

In this Letter we report the previously unobserved influence of the magnetic-field-induced spin reorientation and related symmetry on the linear magnetoelectric effect in Cu_3TeO_6, establishing this material as a playground to study the interplay of spintronics-related phenomena.

High-quality single crystals of Cu_3TeO_6 were grown using HBr chemical transport method in sealed quartz tubes [25] and characterized using an X-ray diffractometer at room temperature. Ferroelectric (FE) polarization hysteresis loops were obtained using a home-made Sawyer-Tower-type virtual ground setup [36] as described in [37] with a frequency set to 77 Hz in a quasi-static electric field up to 500 kV/m [28]. The magnetic properties of Cu_3TeO_6 were studied using Quantum Design (QD) Magnetic Properties Measurement System (MPMS3) magnetometer and vibrating sample magnetometer and torque magnetometer on QD Physical Properties Measurement System.

Our quasi-static electric polarization measurements show that FE polarization is induced by magnetic field in AFM state. $P(E)$ hysteresis loops (Fig. 1) measured in 12 T for $\mathbf{H}\|[001]$ and $\mathbf{E}\|[100]$ in the temperature range from 10 to 70 K below T_N are slightly biased and saturated above 250 kV/m, while above T_N they vanish. Similar behavior is observed for $\mathbf{H}\|[010]$ and $\mathbf{E}\|[100]$ [28].

Saturation polarization P_{sat} dependence on temperature and magnetic field measured for $\mathbf{E}\|[100]$ is shown in Fig. 2. It shows non-zero values for $T \leq T_N$ and $\mathbf{E} \perp \mathbf{H}$ (Fig. 2a). P_{sat} dependence on magnetic field $\mathbf{H}\|[001]$ is linear for temperatures ranging from 15 to 55 K (Fig. 2b). Interestingly, for $\mathbf{H}\|[010]$ and $\mathbf{E}\|[100]$, P_{sat} increases with the field, reaching a maximum at $\mu_0 H = 2.5 - 3$ T and then decreases (Fig. 2c). The ME coupling coefficients obtained at 5 K are $\alpha_{ac} = 0.61$ ps/m, and $\alpha_{ab} = 1.66$ ps/m (in the low-field region) for $\mathbf{H}\|[001]$ and $\mathbf{H}\|[010]$, respectively. Here, we use cubic crystal coordinate system (a, b, c) with $a = [100]$, $b = [010]$ and $c = [001]$ for notation.

The temperature dependence of magnetic susceptibility χ measured in several different magnetic field values for $\mathbf{H}\|[111]$ (Fig. 3a), with a visible kink at $T_N \approx 62$ K, is consistent with the previous findings [25, 30, 31, 38]. Below T_N the susceptibility increases as the field increases, which is typical for AFM materials with multiple orientational domains where the spin reorientation is taking place in the applied magnetic fields [39]. No difference was observed between the zero-field-cooled and field-cooled curves.

The field dependence of magnetization M for $\mathbf{H}\|[001]$ and $\mathbf{H}\|[111]$ measured at 2 K, is presented in Fig. 3b. In the entire range, M seems to be linear in H and isotropic with mild nonlinearity observed for $\mathbf{H}\|[111]$ [28, 40].

In Fig. 3c we plot the angular dependence of magnetic torque $\boldsymbol{\tau}$ in AFM state measured at 2 K in the $([010], [001])$ plane in $\mu_0 H = 15$ T. $\boldsymbol{\tau}$ displays a sharp change of sign for field angles in the vicinity of the [011] direction. Such behavior deviates from the $\tau \propto \sin 2\theta$ dependence expected for AFM with no spin reorientation (solid line in Fig. 3c), and is obtained for $\mu_0 H$ ranging from 1 to 15 T [28].

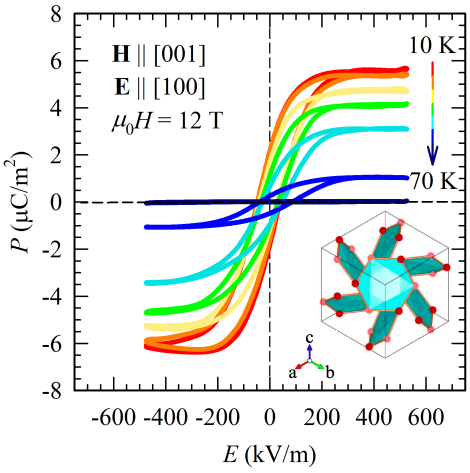

FIG. 1. Ferroelectric contribution to polarization as a function of applied electric field and temperature measured for $\mathbf{H}\|[001]$ and $\mathbf{E}\|[100]$ in applied external magnetic field of 12 T and temperature range from 10 to 70 K in steps of 10 K. Inset: GS AFM structure plotted in unit cell for one of the domains. See supplemental material (SM) [28] for details.

To determine the magnetic structure, we start with the Hamiltonian

$$\mathcal{H} = J_1 \sum_{\langle i,j \rangle} \mathbf{S}_i \cdot \mathbf{S}_j + J_9 \sum_{\langle i,k \rangle} \mathbf{S}_i \cdot \mathbf{S}_k + \\ + d_{DMI} J_1 \sum_{\langle i,j \rangle} \mathbf{d}_{ij} \cdot (\mathbf{S}_i \times \mathbf{S}_j) - \mathbf{H} \cdot \sum_i \hat{\mathbf{g}}_i \cdot \mathbf{S}_i, \quad (1)$$

where J_1 and J_9 are the two dominant isotropic interactions between the first-NN ($d_{\text{Cu–Cu}} = 3.18$ Å) and ninth-NN ($d_{\text{Cu-Cu}} = 6.21$ Å), respectively [32, 41]. Dzyaloshinskii-Moriya interaction (DMI) [42] is introduced between the first-NN. The last term is the Zeeman interaction where $\hat{\mathbf{g}}_i$ is the electron $\mathbf{g}$ tensor of spin i. The orientation of the Dzyaloshinskii-Moriya (DM) unit vector $\mathbf{d}_{ij}$ was obtained from Cu-O-Cu bond geometry [28]. $D = d_{DMI} J_1$ is the magnitude of DMI. The direction of the DMI vector is defined by setting $D > 0$ or $D < 0$, and it has important consequences for the ME effect. The summation for J_1 interaction and DMI goes over first-NN spins and for J_9 over ninth-NN spins where each spin has 4 of both NN [25, 32, 41].

The primitive cell consisting of 12 magnetically inequivalent Cu^{2+} ions fully describes the magnetic structure in Cu_3TeO_6 [25]. We use this primitive cell (Fig. 4a) in our simulations. Next, we map the interactions J_1 and J_9 onto the minimal cell by considering the boundary conditions (see SM [28]). The resulting magnetic lattice

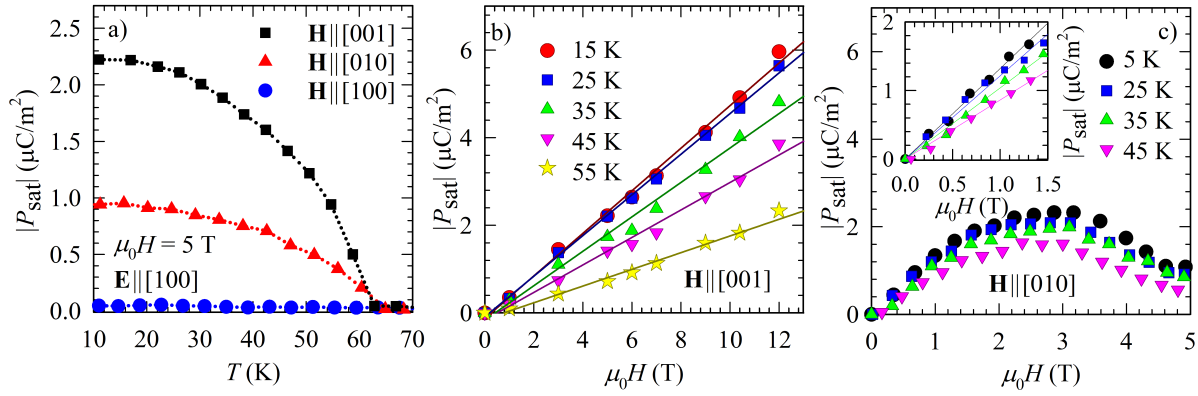

FIG. 2. a) Saturation polarization $P_{\rm sat}$ dependence on temperature for three different orientations of the applied external magnetic field $\mu_0 H = 5$ T with respect to the electric field $\mathbf{E}\|[100]$. b) $P_{\rm sat}$ as a function of magnetic field (0 – 12 T) and temperature (15 – 55 K) measured for $\mathbf{H}\|[001]$ (symbols). Linear fit (lines) gives ME coupling coefficients. c) $P_{\rm sat}$ as a function of magnetic field (0 – 5 T) measured for $\mathbf{H}\|[010]$ (symbols) in the temperature range from 5 to 45 K. Inset: linear fit (lines) for $\mu_0 H \leq 1.5$ T gives ME coupling coefficients at different temperatures.

with interactions J_1 and J_9 mapped onto primitive cell is shown in Fig. 4a. Interestingly, both interactions mapped onto the same lattice result in effective 4 NN which might be a signature of low-dimensionality hidden in this topologically unique 3D magnetic lattice [25, 35].

From the Hamiltonian 1 we write the free energy $\mathcal{F}$

$$\mathcal{F} = \frac{k_B}{g_e^2 \cdot \mu_B \cdot 10^4} \left[J_1 \sum_{\langle i,j \rangle} \mathbf{M}_i \cdot \mathbf{M}_j + J_9 \sum_{\langle i,j \rangle} \mathbf{M}_i \cdot \mathbf{M}_j + d_{DMI} J_1 \sum_{\langle i,j \rangle} \mathbf{d}_{i,j} \left(\mathbf{M}_i \times \mathbf{M}_j \right) \right] - \mathbf{H} \sum_i \hat{\mathbf{g}}_i / g_e \mathbf{M}_i, \quad (2)$$

where k_B is Boltzmann constant, $g_e = 2.0023$ is the free electron g value and μ_B is Bohr magneton. In the minimal cell the summation for both J_1 and J_9 goes over the same pairs $\langle i, j \rangle$ (see Fig. 4a). With $S_0 = 1/2$, and sublattice magnetization for spin i $\mathbf{M}_i = S_0(\sin\theta_i \cos\phi_i, \sin\theta_i \sin\phi_i, \cos\theta_i)$. The calculated $\hat{\mathbf{g}}_i \, \forall i$ is given in SM [28]. θ_i and ϕ_i are polar and azimuthal coordinates with corresponding Cartesian system ([100], [010], [001]). The magnitude of the applied magnetic field H is expressed in Tesla (T) units. We performed calculations with two sets of parameters: 1) $J_1 = J_9 = 4.8$ meV and $D = 0.1 J_1$, proposed from the INS experiment [32], and 2) $J_1 = 7.05$ meV, $J_9 = 3.77$ meV and $D = 0.06 J_1$, proposed from theory [41]. The free energy, Eq. (2), is minimized using the quasi-Newton method. The resulting magnetic structure is used to calculate the total magnetization and torque and to determine the preserved symmetry elements. In this way, the magnetic point group (MPG) was found in zero and finite magnetic fields [44].

The two sets of parameters lead to the same calculated GS, which is shown for one of the 8 AFM domains in Fig. 4a. An excellent agreement is obtained with neutron diffraction experiment [25]. This GS is 8-fold degenerate with 8 AFM domains with dominant spin orientation (easy axis) along ⟨111⟩ directions. The weak canting of spins amounts to $\approx 1^\circ - 2^\circ$, depending on the chosen set of parameters, in good agreement with theory [41]. The magnetic point group of the calculated structure is $\bar{3}'$.

The calculated magnetization per Cu for $\mathbf{H}\|[001]$ and $\mathbf{H}\|[111]$ for two sets of parameters is shown in Fig. 3b, where slightly better agreements is observed for the second set [41]. The calculated magnetic torque τ with parameters from Ref. 32, (Fig. 3c), captures the angular dependence of the measured curves very well. The sharp sign change of τ in the vicinity of [011] direction is observed as a signature of the spin reorientation, as well as the correct phase. The obtained amplitude of torque is, however, 5 times smaller than the one in the experiment, signifying that magnetic anisotropy is underestimated in our model. Increasing the DMI to $D = 0.3 J_1$ almost reproduces the measured amplitude [28]. On the other hand, the torque calculated under the assumption of the GS structure and $\approx 10\%$ domain imbalance (solid line in Fig. 3c) is in stark disagreement with the experiment.

The main result of our analysis is the magnetic-field-induced spin reorientation which is captured by a rotation of the Néel vector $\mathbf{l}$ in applied magnetic field, $\mathbf{l} = (\sum_{i=1}^{6} \mathbf{M}_{i,\uparrow} - \sum_{j=1}^{6} \mathbf{M}_{j,\downarrow})/(12\,M)$, where we distinguish the moments with opposite main components as $\mathbf{M}_{i,\uparrow}$ and $\mathbf{M}_{j,\downarrow}$. For domain i, the direction of $\mathbf{l}_i$ is described by (θ_i, ϕ_i). In Fig. 4b we plot the magnetic phase diagram calculated for $\mathbf{H}\|[001]$ for all domains. The spin reorientation takes place as soon as the finite H is applied. Three phases are observed. A phase with MPG 1 is found for $\mu_0 H_{c0} \lesssim 0.04$ T, a field too low to induce a measurable ME effect. We focus on the two other phases separated by the critical field H_{c1}. The magnetic structures in $\mathbf{H}\|[001]$ for $H_{c0} < H < H_{c1}$ and

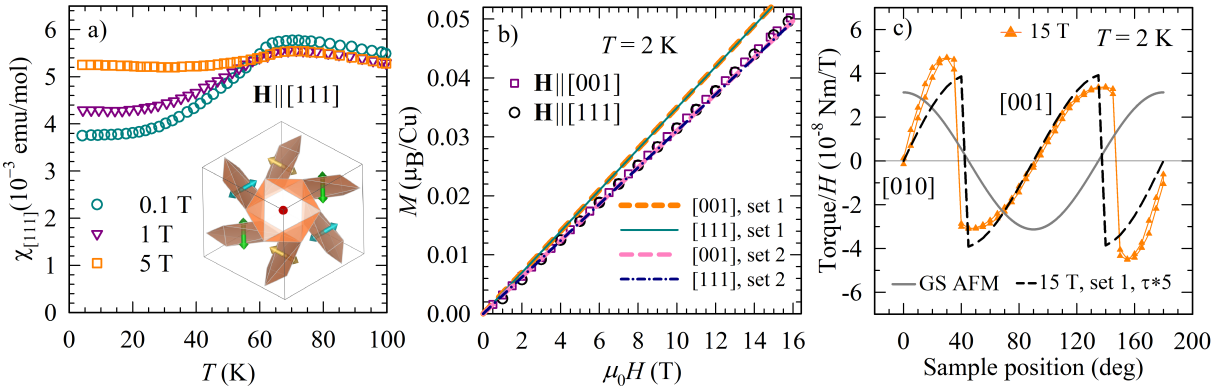

FIG. 3. a) Temperature dependence of magnetic susceptibility in different applied fields for $\mathbf{H}\|[111]$. Inset: schematic of AFM domains in the GS [25, 28, 43]. b) Field dependence of magnetization at $T = 2$ K for $\mathbf{H}\|[001]$ and $\mathbf{H}\|[111]$ (symbols) and calculations (lines). Set 1 and 2 represent the choice of superexchange parameters from Ref. 32 and 41, respectively. c) The angular dependence of magnetic torque $\boldsymbol{\tau}$ measured at $T = 2$ K in the $([010],[001])$ plane (symbols). $\boldsymbol{\tau}$ calculated under the assumption of GS AFM structure (solid line) is compared to $\boldsymbol{\tau}$ calculated from free energy (2) (dashed line). The amplitude of the calculated torque is multiplied by 5 for the latter case.

$H \geq H_{c1}$ are shown in Figs. 4c and 4d respectively. The MPGs of the calculated structures for $H \geq H_{c1}$ depend on the direction of the DM vector, defined by the sign of $D = d_{DMI}J_1$. $D > 0$ gives MPGs in agreement with our polarization measurements. MPGs for $D < 0$ can be found in SM. For $H_{c0} < H < H_{c1}$ the MPG is m ($m \perp \mathbf{H}$), and in $H \geq H_{c1}$ it is $2'm'm$. The magnitude of the critical field $\mu_0 H_{c1}$ amounts to 0.75 T and 0.6 T for the parameters from Refs. 32 and 41, respectively. The $\mu_0 H_{c1} \approx 3$ T suggested from Fig. 2c is reproduced in our model for $D \approx 0.25 J_1$ [28]. Alternatively, another source of magnetic anisotropy energy might be needed to fully capture the magnetic anisotropy of this system.

In table I we list the preserved symmetry operations and the MPGs obtained in our calculations for $D > 0$ [44]. The MPGs obtained for $H > 0$ are polar, in contrast to the nonpolar GS. However, the effect of the field-induced breaking of some symmetries (marked by $\pm$) which would lead to nonpolar MPGs might be too weak to be observable in moderate magnetic fields. We add those nonpolar MPGs in parentheses in table I and Fig. 4b. Among those symmetries is $\bar{1}'$.

All MPGs in table I allow the linear ME effect, while the polar MPGs in $H > 0$ also allow field-induced ferroelectricity and bilinear ME effect [16, 45, 46]. We focus here on the linear ME effect which seems to be the dominant contribution in Cu_3TeO_6. For the GS MPG $\bar{3}'$, tensor $\boldsymbol{\alpha}$ allows finite P for any H direction [28], in disagreement with our results. For α in finite H we refer to table I. For $\mathbf{H}\|[001]$ and $D > 0$ we have [16, 45]

$$\boldsymbol{\alpha}_m = \begin{bmatrix} 0 & 0 & \alpha_{ac} \\ 0 & 0 & \alpha_{bc} \\ \alpha_{ca} & \alpha_{cb} & 0 \end{bmatrix}, \quad \boldsymbol{\alpha}_{2'm'm} = \begin{bmatrix} 0 & 0 & \alpha_{ac} \\ 0 & 0 & 0 \\ \alpha_{ca} & 0 & 0 \end{bmatrix}, \quad (3)$$

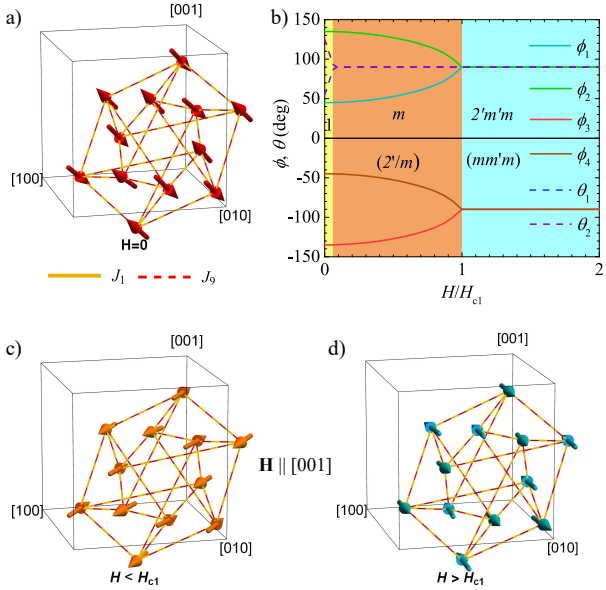

FIG. 4. a) Calculated GS magnetic structure for one domain. b) Magnetic phase diagram obtained for $\mathbf{H}\|[001]$ and $D > 0$. ϕ and θ are azimuthal and polar angles of the calculated Néel vectors. The phases correspond to magnetic structures in c) and d) with MPGs m and $2'm'm$, respectively. c) Calculated magnetic structure for $H_{c0} < H < H_{c1}$ and d) $H \geq H_{c1}$.

which results in $P_{sat,a} = \alpha_{ac} H$ for all H. For $H\|[010]$ and $D > 0$ we have

$$\boldsymbol{\alpha}_m = \begin{bmatrix} 0 & \alpha_{ab} & 0 \\ \alpha_{ba} & 0 & \alpha_{bc} \\ 0 & \alpha_{cb} & 0 \end{bmatrix}, \quad \boldsymbol{\alpha}_{m'm2'} = \begin{bmatrix} 0 & 0 & 0 \\ 0 & 0 & \alpha_{bc} \\ 0 & \alpha_{cb} & 0 \end{bmatrix}, \quad (4)$$

which gives $P_{sat,a} = \alpha_{ab} H$ for $H < H_{c1}$, and $P_{sat,a} = 0$

Symmetry	$\bar{1}'$	**m**	**2**	**m′**	**2′**	**3**	$\bar{3}'$	MPG
$H = 0$	+	-	-	-	-	+	+	$\bar{3}'$
H‖[001]	±	+	-	-	±	-	-	$m\,(2'/m)$
	±	+	±	+	+	-	-	$2'm'm\,(mm'm)$
H‖[001]	±	+	-	-	±	-	-	$m\,(2'/m)$
	±	+	±	+	+	-	-	$m'm2'\,(m'mm)$

TABLE I. The preserved symmetry elements and the corresponding MPGs of the calculated magnetic structure in the GS and in $H > 0$ for $D > 0$. + and − denote preserved and broken symmetries, respectively. ± denotes a symmetry element which is broken but might appear preserved in the experiment, with the corresponding MPGs given in parentheses [28]. Shaded cells represent results for $H \geq H_{c1}$.

for $H \geq H_{c1}$. The same conclusions apply to nonpolar MPGs listed in parentheses in table I. Adding the nonlinear contributions allowed by symmetry results in equivalent conclusions regarding the polarization components (see SM for details). Therefore we conclude that the nonlinear behavior of P_{sat} observed for **H**‖[010] (Fig. 2c) is a consequence of the spin reorientation accompanied by the change of MPG. Our results are supported by a recent paper on the linear ME effect in Cu_3TeO_6 [40].

The static electric polarization and magnetic torque measurements combined with phenomenological simulations demonstrate that magnetic-field-induced spin reorientation accompanied by the change of magnetic point group, needs to be taken into account to understand the linear ME effect observed in Cu_3TeO_6. While the field-induced changes of MPG are reported in other systems, e.g. Cr_2O_3 [47], the transition from the nonpolar AFM GS to polar field-induced state is not common and has been reported only in a few $4f - 3d$ systems [48, 49]. The mechanism of the ME effect in those systems relies on the interaction between the $4f$ and $3d$ magnetic ions. This cannot be applied to Cu_3TeO_6. Our symmetry analysis suggests that the calculated polar structures have weakly differing nonpolar counterparts in moderate magnetic fields, resulting in apparent linearity of the ME effect in Cu_3TeO_6. The nonpolar to polar transition is supported by the strong spin-phonon coupling [29, 30] and very slow AFM domain dynamics observed in Cu_3TeO_6 in weak magnetic field [25], and the mechanism is probably rooted in the strong spin-lattice coupling which is not accounted for in our analysis. The change of magnetic symmetry in the applied magnetic field is critical to consider in further studies of the topological properties of Cu_3TeO_6 and similar topological antiferromagnets.
After the submission of this work, two papers reported linear ME effect in Cu_3TeO_6 [40, 50]. The authors were not aware of the spin reorientation in nonzero magnetic field. Their results support the symmetry analysis presented in this work.

This work was supported by the Croatian Science Foundation (Grant IP-2018-01-2730) and projects Cryogenic Centre at the Institute of Physics - KaCIF (Grant KK.01.1.1.02.0012) and Centre for Advanced Research of Complex Systems CeNIKS (Grant KK.01.1.1.02.0013), co-financed by the Croatian Government and the European Union through the European Regional Development Fund - Competitiveness and Cohesion Operational Programme. V. K. and D. D. acknowledge funding of Croatian Science Foundation through grant HRZZ DOK-09-2018. X. R. acknowledges funding from the French National Research Agency (ANR - Grant ANR-19-CE08-0013-02; HTHPCM Project) and GENCI for granting access to the HPC resources of [TGCC/CINES/IDRIS] under the allocation 2022-A0130907682.

* vkisicek@ifs.hr
† mirta@ifs.hr

[1] V. Baltz, A. Manchon, M. Tsoi, T. Moriyama, T. Ono, and Y. Tserkovnyak, Rev. Mod. Phys. **90**, 015005 (2018).
[2] A. Barman *et al.*, J. Phys.: Condens.Matter **33**, 413001 (2021).
[3] C. Song, Y. You, X. Chen, X. Zhou, Y. Wang, and F. Pan, Nanotechnology **29**, 112001 (2018).
[4] T. Jungwirth, X. Marti, P. Wadley, and J. Wunderlich, Nat. Nanotechnol. **11**, 231 (2016); T. Jungwirth, J. Sinova, A. Manchon, X. Marti, J. Wunderlich, and C. Felser, Nat. Phys. **14**, 200 (2018).
[5] M. Malki and G. S. Uhrig, Europhys. Lett. **132**, 20003 (2020); P. A. McClarty, Annu. Rev. Condens. Matter Phys. **13**, 171 (2022); B. A. Bernevig, C. Felser, and H. Beidenkopf, Nature **603**, 41–51 (2022).
[6] L. Šmejkal, Y. Mokrousov, B. Yan, and A. H. MacDonald, Nat. Phys. **14**, 242 (2018); V. Bonbien, F. Zhuo, A. Salimath, O. Ly, A. Abbout, and A. Manchon, J. Phys. D: Appl. Phys. **55**, 103002 (2022).
[7] D. I. Khomskii, ECS J. Solid State Sci. Technol. **11**, 054004 (2022).
[8] M. Norman, J. Magn. Magn. Mater. **452**, 507 (2018).
[9] T. Vuletić, B. Korin-Hamzić, T. Ivek, S. Tomić, B. Gorshunov, M. Dressel, and J. Akimitsu, Phys. Rep. **428**, 169 (2006).
[10] C. Proust and L. Taillefer, Annu. Rev. Condens. Matter Phys. **10**, 409 (2019).
[11] S. Dong, H. Xiang, and E. Dagotto, Natl. Sci. Rev. **6**, 629 (2019).
[12] M. Fiebig, J. Phys. D: Appl. Phys. **38**, 123 (2005).
[13] N. A. Spaldin and R. Ramesh, Nat. Mater. **18**, 203 (2019).
[14] F. Thöle, A. Keliri, and N. A. Spaldin, J. Appl. Phys. **127**, 213905 (2020).
[15] J.-P. Rivera, Eur. Phys. J. B **7**, 299 (2009).
[16] H. Schmid, J. Phys.: Condens.Matter **20**, 434201 (2008).
[17] N. Ortega, A. Kumar, J. F. Scott, and R. S. Katiyar, J. Phys.: Condens.Matter **27**, 504002 (2015).
[18] N. A. Spaldin, Proc. R. Soc. A **476**, 20190542 (2020).
[19] N. A. Hill, J. Phys. Chem. B **104**, 6694 (2000).
[20] Y. Tokura, S. Seki, and N. Nagaosa, Rep. Prog. Phys.

77, 076501 (2014).
[21] S. Dong, J.-M. Liu, S.-W. Cheong, and Z. Ren, Adv. Phys. **64**, 519 (2015).
[22] M. Fiebig, T. Lattermoser, D. Meier, and M. Trassin, Nat. Rev. Mater. **1**, 16046 (2016).
[23] T. H. Arima, J. Phys. Soc. Jpn. **80**, 052001 (2011).
[24] L. Falck, O. Lindqvist, and J. Moret, Acta Crystallogr., Sect. B **34**, 896 (1978).
[25] M. Herak, H. Berger, M. Prester, M. Miljak, I. Živković, O. Milat, D. Drobac, S. Popović, and O. Zaharko, J. Phys.: Condens. Matter **17**, 7667 (2005).
[26] M. Herak, Solid State Commun. **151**, 1588 (2011).
[27] K. Li, C. Li, J. Hu, Y. Li, and C. Fang, Phys. Rev. Lett. **119**, 247202 (2017).
[28] The supplemental material provides the details on the polarization and torque results, the antiferromagnetic order with domains, the phenomenological calculation of the magnetic states and the determined symmetries, as well as magnetoelectric tensor for the different magnetic point groups, and includes Refs. [51–53].
[29] Caimi, G., Degiorgi, L., Berger, H., and Forró, L., Europhys. Lett. **75**, 496 (2006).
[30] K. Y. Choi, P. Lemmens, E. S. Choi, and H. Berger, J. Phys.: Condens.Matter **20**, 505214 (2008).
[31] S. Bao, J. Wang, W. Wang, Z. Cai, S. Li, Z. Ma, D. Wang, K. Ran, Z.-Y. Dong, D. L. Abernathy, S.-L. Yu, X. Wan, J.-X. Li, and J. Wen, Nat. Commun. **9**, 2591 (2018).
[32] W. Yao, C. Li, L. Wang, S. Xue, Y. Dan, K. Iida, K. Kamazawa, K. Li, C. Fang, and Y. Li, Nature Phys. **14**, 1011–1015 (2018).
[33] S. Bao, Z. Cai, W. Si, W. Wang, X. Wang, Y. Shangguan, Z. Ma, Z.-Y. Dong, R. Kajimoto, K. Ikeuchi, S.-L. Yu, J. Sun, J.-X. Li, and J. Wen, Phys. Rev. B **101**, 214419 (2020).
[34] L. Chen, M.-E. Boulanger, Z.-C. Wang, F. Tafti, and L. Taillefer, Proc. Natl. Acad. Sci. U. S. A. **119**, e2208016119 (2022).
[35] S.-H. Baek, H. W. Yeo, J. Park, K.-Y. Choi, and B. Büchner, Phys. Rev. Res. **3**, 033109 (2021).
[36] K. Prume, T. Schmitz, and S. Tiedke, Electrical characterization of ferroelectrics, in *Polar Oxides* (John Wiley and Sons, Ltd, Weinheim, Germany, 2004) Chap. 3, pp. 53–75.
[37] M. Dragičević, D. R. Góngora, Ž. Rapljenović, M. Herak, V. Brusar, D. Altus, M. Pregelj, A. Zorko, H. Berger, D. Arčon, and T. Ivek, Phys. Rev. B **104**, L121107 (2021).
[38] Z. He and M. Itoh, J. Magn. Magn. Mater. **354**, 146 (2014).
[39] L. Zhao, H. Guo, W. Schmidt, K. Nemkovski, M. Mostovoy, and A. C. Komarek, Phys. Rev. B **96**, 054424 (2017).
[40] Y. Tang, L. Lin, G. Zhou, W. Zhai, L. Huang, J. Zhang, S. Zheng, M. Liu, Z. Yan, X. Jiang, X. Li, and J.-M. Liu, Phys. Rev. B **107**, 214416 (2023).
[41] D. Wang, X. Bo, F. Tang, and X. Wan, Phys. Rev. B **99**, 035160 (2019).
[42] I. Dzyaloshinsky, J. Phys. Chem. Solids **4**, 241 (1958); T. Moriya, Phys. Rev. **120**, 91 (1960).
[43] K. Momma and F. Izumi, J. Appl. Crystallogr. **44**, 1272 (2011).
[44] M. I. Aroyo, J. M. Perez-Mato, C. Capillas, E. Kroumova, S. Ivantchev, G. Madariaga, A. Kirov, and H. Wondratschek, Z. fur Krist. - Cryst. Mater. **221**, 15 (2006); M. I. Aroyo, J. M. Perez-Mato, D. Orobengoa, E. Tasci, G. de la Flor, and A. Kirov, Bulg. Chem. Commun. **43**, 183 (2011); D. B. Litvin, *Magnetic Group Tables: 1-, 2- and 3-Dimensional Magnetic Subperiodic Groups and Magnetic Space Groups* (International Union of Crystallography, Chester, England, 2013).
[45] R. E. Newnham, *Properties of Materials (Anisotropy, Symmetry, Structure)* (Oxford University Press, New York, USA, 2005).
[46] S. V. Gallego, J. Etxebarria, L. Elcoro, E. S. Tasci, and J. M. Perez-Mato, Acta Crystallographica Section A **75**, 438 (2019).
[47] M. Fiebig, D. Fröhlich, and H. J. Thiele, Phys. Rev. B **54**, R12681 (1996).
[48] X. Shen, L. Zhou, Y. Chai, Y. Wu, Z. Liu, Y. Yin, H. Cao, C. D. Cruz, Y. Sun, C. Jin, A. Muñoz, J. A. Alonso, and Y. Long, npg Asia Materials **11**, 50 (2019).
[49] P. Yanda, F. Orlandi, P. Manuel, N. Boudjada, J. Rodriguez-Carvajal, and A. Sundaresan, Phys. Rev. B **104**, 144401 (2021).
[50] A. Shahee, K. Yoo, B. Koteswararao, N. V. Ter-Oganessian, and K. H. Kim, Front. Mater. **10**, 01 (2023).
[51] J. Chakraborty, J. Phys. Chem. Solids **134**, 182 (2019).
[52] F. Keffer, Phys. Rev. **126**, 896 (1962).
[53] K. Koepernik and H. Eschrig, Phys. Rev. B **59**, 1743 (1999).